**Seventh International Conference on Computational Fluid Dynamics (ICCFD7), Big Island, Hawaii, July 9-13, 2012**

**ICCFD7-1906**

# Detached-Eddy Simulation Based on the $v^2$-$f$ Model

SolKeun Jee* and Karim Shariff*
Corresponding author: solkeun.jee@nasa.gov
* NASA Ames Research Center, Moffett Field, CA, USA.

**Abstract:** Detached-eddy simulation (DES) based on the $v^2$-$f$ Reynolds-averaged Navier-Stokes (RANS) model is developed and tested. The $v^2$-$f$ model incorporates the anisotropy of near-wall turbulence, which is absent in other RANS models commonly used in the DES community. The $v^2$-$f$ RANS model is modified in order that the proposed $v^2$-$f$-based DES formulation reduces to a transport equation for the subgrid-scale kinetic energy in isotropic turbulence. First, three coefficients in the elliptic relaxation equation are modified, which is tested in channel flow with friction Reynolds numbers up to 2000. Then, the proposed $v^2$-$f$ DES model formulation is derived. The constant, $C_{\mathrm{DES}}$, required in the DES formulation was calibrated by simulating both decaying and statistically-steady isotropic turbulence. After $C_{\mathrm{DES}}$ is calibrated, the $v^2$-$f$ DES formulation is tested for flow around a circular cylinder at a Reynolds number of 3900, in which case turbulence develops after separation. Simulations indicate that this model represents the turbulent wake nearly as accurately as the dynamic Smagorinsky model. For comparison, Spalart-Allmaras-based DES is also included in the cylinder flow simulation.

*Keywords:* detached-eddy simulation, $v^2$-$f$ model, hybrid RANS/LES.

## 1 Introduction

Detached-eddy simulation (DES) [1, 2, 3] is a hybrid RANS/LES approach that performs RANS in attached regions and LES in detached regions using a single model. In the LES region, the length scale of the model is set proportional to the grid size $\Delta$. The RANS model thereby becomes an LES model.

The $v^2$-$f$-based DES approach developed here incorporates more flow physics in RANS mode than Spalart-Allmaras(SA)-based DES [3], which is widely used. Firstly, the near-wall damping of SA RANS [4] does not distinguish between velocity components. In contrast, the $v^2$-$f$ formulation [5] models the suppression of wall normal velocity fluctuation caused by non-local pressure-strain effects. This anisotropy has been shown to improve prediction of separation and reattachment [6, 7, 8]. Among the few works where both $v^2$-$f$ and SA RANS were compared, Iaccarino et al. [7] predicted the pressure coefficient $C_p$ more accurately with $v^2$-$f$ than SA for flow over a 2D hump with steady-suction flow control. Constantinescu et al. [8] obtained an accurate friction coefficient $C_f$ on a sphere after laminar separation with $v^2$-$f$ but an inaccurate prediction with the $k$-$\omega$, $k$-$\epsilon$, and SA RANS models. Secondly, the SA model uses the minimum distance to the wall as the turbulence length scale which is not necessarily accurate at or near separation. The $v^2$-$f$ model, on the other hand, computes a length scale based on flow properties (namely, the kinetic energy $k$, the dissipation rate $\epsilon$, and the kinematic viscosity $\nu$). In LES mode, the present $v^2$-$f$ DES model gives a transport equation for subgrid-scale (sgs) kinetic energy which is less empirical than the sgs viscosity transport equation used in SA-based DES.

A brief summary of the proposed $v^2$-$f$ DES methodology is as follows. The $v^2$-$f$ RANS model [5] has transport equations for $k$, $\epsilon$, and $\overline{v^2}$ together with an elliptic relaxation equation for a function $f$. These equations contain length and time scales $L$ and $T$. The choice between RANS and LES modes is made by setting these scales appropriately. When the grid is fine enough to capture large-scale turbulent eddies, in particular, when $C_{\mathrm{DES}}\Delta < k^{3/2}/\epsilon$, LES mode is selected. Otherwise, RANS mode is selected. As suggested by Spalart et al. [1], the coefficient $C_{\mathrm{DES}}$ is chosen to match the correct energy spectrum in isotropic turbulence. In LES mode, the time scale is set to $T = C_{\mathrm{DES}}\Delta/\sqrt{k}$ where $k$ now represents the sgs kinetic

energy. In principal, a $k$ equation is sufficient together with $\Delta$ to provide a subgrid viscosity. However, the $v^2$-$f$ model bases its eddy viscosity on $\overline{v^2}$ (see (1)), and therefore, even in LES mode, the $\overline{v^2}$ transport equation and elliptic equation for $f$ play a role. Only the $\epsilon$ does not play a role in LES mode. As discussed later, the $v^2$-$f$ model [5] is modified so that, for isotropic turbulence, the entire set of equations reduces to a transport equation for the sgs $k$. In particular, coefficients in the elliptic relaxation equation are modified so that the $\overline{v^2}$ transport equation becomes approximately 2/3 times the $k$ transport equation in the limit of LES for isotropic turbulence.

The proposed $v^2$-$f$ DES model is described in section 2. In section 3, results for this model are compared with the dynamic Smagorinsky model [9] and SA-based delayed DES [2] using the same flow solver and grid for flow past a cylinder at a Reynolds number based on the diameter of 3900. This test is not chosen to determine which DES model is better than others, since it is expected that all DES models will behave like the Smagorinsky model for this flow. Conclusions are presented in section 4.

## 2 $v^2$-$f$ DES Model

The DES model proposed is based on Lien et al.'s version of the $v^2$-$f$ RANS model [5]. The quantity $\overline{v^2}$ should be interpreted as a velocity scalar, not a Reynolds stress tensor component; the function $f$ makes $\overline{v^2}$ behave like the wall normal component of the Reynolds stress $\langle u_n' u_n' \rangle$ [6]. A condition we have imposed on $\overline{v^2}$ is that in isotropic turbulence $\overline{v^2}$ should be the average of the normal components of the Reynolds stress. This assumption allows us to formulate a DES model that reduces to a transport equation for sgs-$k$ in isotropic turbulence. The derivation below starts from the $v^2$-$f$ RANS Eqs.(1)-(5). To reach the final formulation (Eqs.(18)-(22)), the formulations of sgs-$k$ LES (Eqs.(12)-(14)) and $k$-$\epsilon$ DES (Eqs.(15)-(17)) are derived on the way.

The $v^2$-$f$ RANS model of Lien et al. [5] is

$$\begin{aligned}
\nu_t &= c_\mu \overline{v^2} T_{\mathrm{RANS}} && (1)\\
\partial_t k + U_j \partial_j k &= \mathcal{P} - \epsilon + \partial_j \left[ (\nu + \nu_t)\, \partial_j k \right] && (2)\\
\partial_t \epsilon + U_j \partial_j \epsilon &= \frac{c_{\epsilon 1}\mathcal{P} - c_{\epsilon 2}\epsilon}{T_{\mathrm{RANS}}} + \partial_j \left[ \left( \nu + \frac{\nu_t}{\sigma_\epsilon} \right) \partial_j \epsilon \right] && (3)\\
\partial_t \overline{v^2} + U_j \partial_j \overline{v^2} &= k f - 6 \frac{\overline{v^2}}{k} \epsilon + \partial_j \left[ (\nu + \nu_t)\, \partial_j \overline{v^2} \right] && (4)\\
c_L^2 L_{\mathrm{RANS}}^2 \nabla^2 f - f &= \frac{1}{T_{\mathrm{RANS}}} \left[ (c_1 - 6) \frac{\overline{v^2}}{k} - \frac{2}{3}(c_1 - 1) \right] - c_2 \frac{\mathcal{P}}{k}, && (5)
\end{aligned}$$

where the time and length scales are defined by

$$T_{\mathrm{RANS}} = \min \left[ \max \left[ \frac{k}{\epsilon}, c_T \left( \frac{\nu}{\epsilon} \right)^{1/2} \right], \frac{0.6k}{\sqrt{6} C_\mu \overline{v^2} |S_{ij}|} \right], \; L_{\mathrm{RANS}} = \max \left[ \min \left[ \frac{k^{3/2}}{\epsilon}, \frac{k^{3/2}}{\sqrt{6} C_\mu \overline{v^2} |S_{ij}|} \right], c_\eta \left( \frac{\nu^3}{\epsilon} \right)^{1/4} \right]. \quad (6)$$

Note that the realizability constraints of Durbin [10], devised to avoid the stagnation point anomaly, are imposed on both scales [11]. The turbulence production $\mathcal{P} \equiv 2\nu_t |S_{ij}|^2$, and the strain rate tensor $S_{ij} \equiv \frac{1}{2}(\partial_j U_i + \partial_i U_j)$. The coefficients are given by

$$\begin{gathered}
c_\mu = 0.22, \quad c_{\epsilon 1} = 1.4 \left( 1 + 0.045 \sqrt{k/\overline{v^2}} \right), \quad c_{\epsilon 2} = 1.9, \quad \sigma_\epsilon = 1.3, \\
c_1 = 1.4, \quad c_2 = 0.3, \quad c_T = 6, \qquad c_L = 0.23, \quad c_\eta = 70. \quad (7)
\end{gathered}$$

Wall boundary conditions are

$$k_w = 0, \quad \epsilon_w = \nu \partial_n^2 k|_w, \quad \overline{v_w^2} = 0, \quad f_w = 0, \quad (8)$$

where $\partial_n$ is the wall-normal gradient. Note that in Eq.(5), we have chosen to keep $c_L$ outside of the definition

of $L_{\rm RANS}$ for a later purpose, unlike Lien et al. [5].

To begin with, we modify the three coefficients in the elliptic relaxation equation (5) as follows,

$$c_2 = c_{2,0} + \tfrac{1}{2}(2/3 - c_{2,0})\left[1 + \tanh\left\{c_{2,1}(\overline{v^2}/k - c_{2,2})\right\}\right],\ c_{2,0} = 0.3,\ c_{2,1} = 50,\ c_{2,2} = 0.55 \tag{9}$$

$$c_L = 0.115, \quad c_\eta = 140 \tag{10}$$

The value of $c_{2,0}$ is the unmodified value of $c_2$. The other parameters $c_{2,1}$ and $c_{2,2}$ are chosen such that $c_2 \to 2/3$ when $\overline{v^2}/k \gtrsim 0.6$, as shown in Fig. 1. This increases the rapid distribution term (the last term in Eq. (5)) so that it reduces to the isotropization of production (IP) model [12] when $c_2 = 2/3$. The parameters $c_{2,1}$ and $c_{2,2}$, which determine the rate and location of the transition region in the tanh function, have not been optimized. The modification of $c_2$ allows $\overline{v^2}$ to be approximately $(2/3)k$ when this model is used as an sgs model for isotropic turbulence.

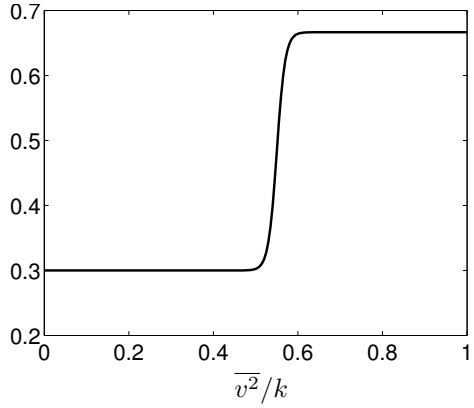


Figure 1: The modified $c_2$ of the present $v^2$-$f$ RANS model

We show that if $\overline{v^2}/k = 2/3$ initially, it remains so approximately because the $\overline{v^2}$ equation (4) is about $2/3$ of the $k$ equation (2). Let us approximate $f$ as $\tilde{f}$ where $\tilde{f}$ is defined by

$$\begin{aligned} \tilde{f} &\equiv \frac{\epsilon}{k}\left[(c_1 - 6)\frac{\overline{v^2}}{k} - \frac{2}{3}(c_1 - 1)\right] + c_2\frac{\mathcal{P}}{k} \\ &= 5\frac{\overline{v^2}}{k^2}\epsilon + c_2\frac{\mathcal{P}}{k}, \quad \text{if} \quad \overline{v^2}/k = 2/3 \end{aligned} \tag{11}$$

This approximation is valid for $y^+ \gtrsim 10$ in channel flow, as shown in Fig. 2. The channel flow simulation is discussed in detail below. Substituting this approximation into Eq. (4), the right-hand side of the $\overline{v^2}$ equation (4) becomes $2/3$ of the $k$ equation (2) because $c_2 \to 2/3$. It was found that the modified $c_2$ (Eq. (9)) required $c_L$ and $c_\eta$ to also be modified to yield acceptable results for channel flow. The value of the product $c_L c_\eta = 16.1$ remains the same in order to keep the Laplacian term near the wall the same as in the unmodified form and to reduce it away from wall.

To validate the modified coefficients of the elliptic relaxation equation, fully developed turbulent channel flow with friction Reynolds numbers $Re_\tau$ up to 2000 are simulated in RANS mode and compared with DNS [13, 14, 15, 16]. Figure 3 shows that this modification maintains the performance of the unmodified RANS model with a slightly better prediction of $\overline{v^2}$ near the center.

In the DES approach, a RANS model switches to an LES model based on a comparison of length scales. The LES length scale is determined by the grid size $\Delta$, so only a time scale equation is needed. We would like the $v^2$-$f$ DES model to reduce to an sgs-$k$ equation model similar to Yoshizawa's model [17] for isotropic turbulence given that for isotropic turbulence $\left\langle\overline{v^2}\right\rangle$ becomes the average of the sgs normal stress

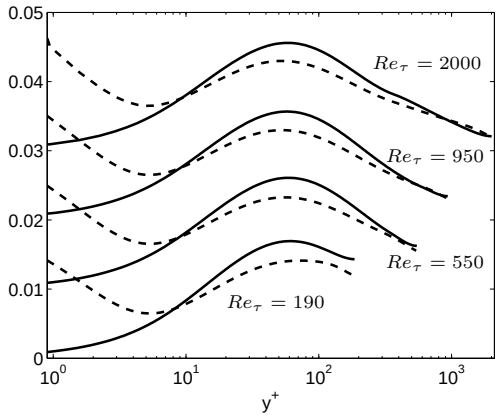


Figure 2: The function $f^+$ (—) and its approximation $\tilde{f}^+ = 5\overline{v^2}^+\epsilon^+/{k^+}^2 + c_2\mathcal{P}^+/k^+$ i.e., Eq.(11) (- -) in the present $v^2$-$f$ RANS for the channel. The profiles for $Re_\tau = 550$, $Re_\tau = 950$ and $Re_\tau = 2000$ are shifted upward along the vertical axis by 0.01, 0.02 and 0.03, respectively. The plus superscript indicates wall units.

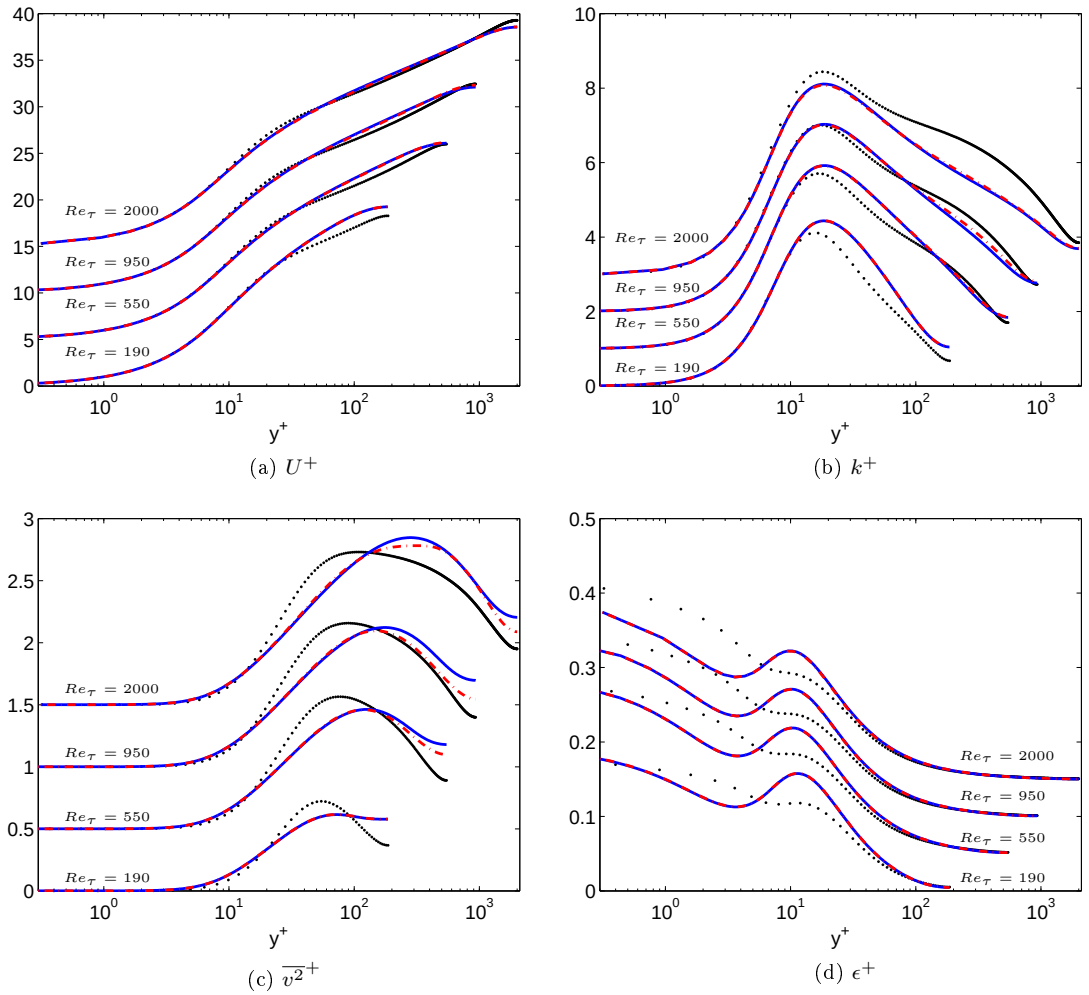


Figure 3: Comparison of DNS (dots) and RANS with the unmodified [5] (—) and the present $v^2$-$f$ model (– · –) in turbulent channel flow. The plus superscript indicates wall units.

i.e., $\left\langle \overline{v^2} \right\rangle = (2/3)\langle k \rangle$, where the angle bracket $\langle\rangle$ denotes an ensemble/time average. An sgs-$k$ LES model is

$$\nu_t = c_\mu \frac{2}{3} k T_{\rm LES}, \quad T_{\rm LES} = \frac{k}{\epsilon_{\rm LES}} \tag{12}$$

$$\partial_t k + U_j \partial_j k = \mathcal{P} - \epsilon_{\rm LES} + \partial_j \left[ (\nu + \nu_t) \partial_j k \right] \tag{13}$$

$$\epsilon_{\rm LES} = \frac{k^{3/2}}{L_{\rm LES}}, \quad L_{\rm LES} = C_{\rm DES} \Delta \tag{14}$$

When the flow is in equilibrium i.e., $\mathcal{P} = \epsilon_{\rm LES}$, a Smagorinsky-like eddy viscosity $\nu_t \propto |S_{ij}| \Delta^2$ is obtained.

As an intermediate step towards the $v^2$-$f$ DES model, a simplified $k$-$\epsilon$ based DES model (without damping functions) is presented. Incorporating the dissipation equation into the DES context yields

$$\nu_t = c_\mu \frac{2}{3} k T_{\rm DES}, \quad T_{\rm DES} = L_{\rm DES}/\sqrt{k}, \quad L_{\rm DES} = \min[k^{3/2}/\epsilon, \underbrace{C_{\rm DES}\Delta}_{L_{\rm LES}}] \tag{15}$$

$$\partial_t k + U_j \partial_j k = \mathcal{P} - \epsilon_{\rm DES} + \partial_j \left[ (\nu + \nu_t) \partial_j k \right], \quad \epsilon_{\rm DES} = k^{3/2}/L_{\rm DES} \tag{16}$$

$$\partial_t \epsilon + U_j \partial_j \epsilon = \frac{c_{\epsilon 1}\mathcal{P} - c_{\epsilon 2}\epsilon}{T_{\rm DES}} + \partial_j \left[ \left( \nu + \frac{\nu_t}{\sigma_\epsilon} \right) \partial_j \epsilon \right] \tag{17}$$

If the RANS length scale is selected, then $T_{\rm DES} = k/\epsilon$ and $\epsilon_{\rm DES} = \epsilon$ as expected. Otherwise, $T_{\rm DES} = k/\epsilon_{\rm LES}$ which is the same as $T_{\rm LES}$ in Eq.(12), and Eqs.(15)-(17) reduce to Eqs.(12)-(14).

Finally, to present the full $v^2$-$f$ DES model, the $\overline{v^2}$ and $f$ equations are included in the complete set of equations:

$$\nu_t = c_\mu \overline{v^2} T_{\rm DES} \tag{18}$$

$$\partial_t k + U_j \partial_j k = \mathcal{P} - \epsilon_{\rm DES} + \partial_j \left[ (\nu + \nu_t) \partial_j k \right] \tag{19}$$

$$\partial_t \epsilon + U_j \partial_j \epsilon = \frac{c_{\epsilon 1}\mathcal{P} - c_{\epsilon 2}\epsilon}{T_{\rm DES}} + \partial_j \left[ \left( \nu + \frac{\nu_t}{\sigma_\epsilon} \right) \partial_j \epsilon \right] \tag{20}$$

$$\partial_t \overline{v^2} + U_j \partial_j \overline{v^2} = k f - 6 \frac{\overline{v^2}}{k} \epsilon_{\rm DES} + \partial_j \left[ (\nu + \nu_t) \partial_j \overline{v^2} \right] \tag{21}$$

$$c_L^2 L_{\rm DES}^2 \nabla^2 f - f = \frac{1}{T_{\rm DES}} \left[ (c_1 - 6) \frac{\overline{v^2}}{k} - \frac{2}{3}(c_1 - 1) \right] - c_2 \frac{\mathcal{P}}{k} \tag{22}$$

$$\text{RANS mode} : \text{ if } k^{3/2}/\epsilon < L_{\rm LES}, \text{ then } L_{\rm DES} = L_{\rm RANS}, \ T_{\rm DES} = T_{\rm RANS}, \text{ and } \epsilon_{\rm DES} = \epsilon \tag{23}$$

$$\text{LES mode} : \text{ otherwise, } L_{\rm DES} = C_{\rm DES}\Delta, \ T_{\rm DES} = C_{\rm DES}\Delta/\sqrt{k}, \text{ and } \epsilon_{\rm DES} = k^{3/2}/(C_{\rm DES}\Delta), \tag{24}$$

where $T_{\rm RANS}$ and $L_{\rm RANS}$ are defined in Eq.(6). Note that $(2/3)k$ appears in Eqs.(12) and (15) but $\overline{v^2}$ appears in Eq.(18). For an LES simulation of isotropic turbulence, $\overline{v^2}$, if interpreted as the sgs average normal stress, should be statistically $(2/3)k$. The modified $c_2$ in Eq.(9) provides this behavior. Simulations indicate that the unmodified $c_2 = 0.3$ yields $\left\langle \overline{v^2} \right\rangle / \langle k \rangle \simeq 0.4$ for isotropic turbulence.

Note that the Kolmogorov length scale present in Eq. (6) is not considered in the length comparison in Eqs. (23) and (24) because it is expected that, near the RANS and LES transition (or away from the wall), the RANS length scale will be $k^{3/2}/\epsilon$. However, a discontinuity in the length or time scale may occur at the RANS/LES transition if the Kolmogorov length scale happens to be the RANS scale. This would occur in low-$Re$ flows. One way to avoid such a discontinuity is to use $L_{\rm RANS}$ for the length scale comparison. This alternative is not considered here because it turns off the realizability constraints in Eq. (6) causing the stagnation point anomaly [10] near the front stagnation point on a cylinder. Flow simulation over a cylinder is discussed in section 3.

The proposed DES model is implemented in the Stanford incompressible Navier-Stokes solver CDP (v2.3). This code is based on finite-volume spatial discretization with second-order accuracy and a second-

order implicit fractional step method [18, 19]. CDP employs a novel collocated formulation to conserve mass, momentum and kinetic energy approximately (in the inviscid limit) on hybrid unstructured meshes. The second-order central difference scheme is used for both the convection and diffusion terms of the momentum equation. The scalar transport equations (19)-(21) are time advanced implicitly. To achieve numerical stabilization for the scalar equations, which are significantly controlled by the source terms, the convective terms in these equations are discretized with the 1st-order upwind scheme. The diffusion term in each scalar equation is discretized with the central scheme. In the test of isotropic turbulence, when this upwind scheme is used for the scalar convection term only, it yields the identical energy spectrum compared to use of the central scheme for all the terms. An upwind-biased scheme is never used for the momentum equation in this study.

To calibrate $C_{\mathrm{DES}}$, decaying isotropic turbulence is considered. The initial field uses the $512^3$ DNS data of Wray [20] at $Re_\lambda = 105$ sampled down to $32^3$ or $64^3$. The computational cube has sides $L_{\mathrm{box}} = 2\pi$ with periodic boundary conditions in the three directions. Quantities in the DES model are initialized by running for some time with a frozen initial velocity field. The flow is allowed to run about 3.7 and 10.7 large-eddy turnover times at which point $Re_\lambda = 65$ and $Re_\lambda = 61$, respectively. The large-eddy turnover timescale is determined by the longitudinal length scale $L_{11}$ and the r.m.s. velocity fluctuation $u_{\mathrm{rms}}$ computed from the DNS data at $Re_\lambda = 105$ (the initial state).

Figs. 4a and 4b show the energy spectrum with three values of $C_{\mathrm{DES}}$. The $v^2$-$f$ DES simulation with $C_{\mathrm{DES}} = 0.8$ agrees very well with DNS [20] and experiments [21] up to the cut-off wave number at the later instant when $Re_\lambda = 61$ (Fig. 4b). $v^2$-$f$ DES gives almost exactly the same energy spectrum as produced by the dynamic Smagorinsky model (Figs. 4c and 4d). In Figs. 4e and 4f, all three formulations, namely, sgs-$k$ LES, $k$-$\epsilon$ DES, and $v^2$-$f$ DES, give the same energy spectrum with the same $C_{\mathrm{DES}}$. This indicates that the $v^2$-$f$ DES formulation indeed reduces to the others. The coefficient $C_{\mathrm{DES}} = 0.8$ is used for the rest of the paper.

Because it allows a higher Reynolds number and a wider inertial range, forced isotropic turbulence at $Re_\lambda = 98$ is also considered using the stochastic forcing of Eswaran and Pope [22]. The computational cube has the same size $L_{\mathrm{box}} = 2\pi$ as the decaying case. The radius of the sphere of forced wavenumbers is $K_F = \sqrt{8}$, giving a total 92 forced modes. The forcing amplitude and the forcing autocorrelation time scale are chosen as $\sigma = 0.3572$ and $T_L = 0.4312$, respectively, following the nomenclature of Ref. [22]. Initial conditions are not relevant, since the flow is driven to a statistical steady state. The grid is $128^3$ for the present DNS, and two grids of $16^3$ and $32^3$ are used for LES with the dynamic Smagorinsky model and $v^2$-$f$ DES. Statistics were obtained by averaging over samples collected over 30 eddy turnover times in the steady state which is reached after 10 eddy turnover times from the initial condition. The velocity-derivative skewness $S = 1/3 \left[ \left\langle (\partial_i u_i)^3 \right\rangle / \left\langle (\partial_j u_j)^2 \right\rangle^{3/2} \right]$ has values ($\sim 0.45$) typical of isotropic turbulent at $Re_\lambda \sim 100$ [23]. The $v^2$-$f$ DES simulation gives almost exactly the same energy spectrum as produced by the dynamic Smagorinsky model (Fig. 5). Forced isotropic turbulence had not been used for the $C_{\mathrm{DES}}$ calibration in the DES community. This simulation shows that the forced case is an alternative for this calibration.

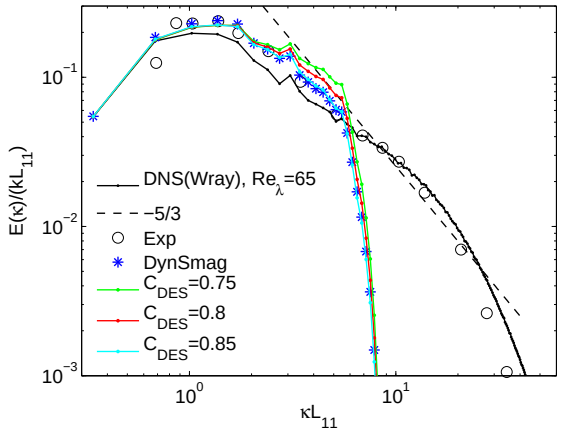


(a) $v^2$-$f$ DES with three different $C_{\mathrm{DES}}$ at $Re_\lambda = 65$

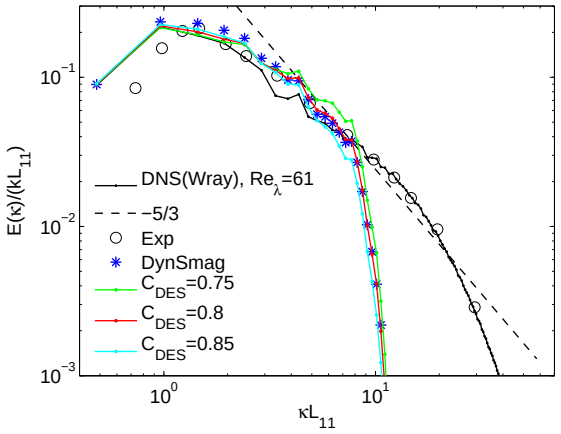


(b) $v^2$-$f$ DES with three different $C_{\mathrm{DES}}$ at $Re_\lambda = 61$

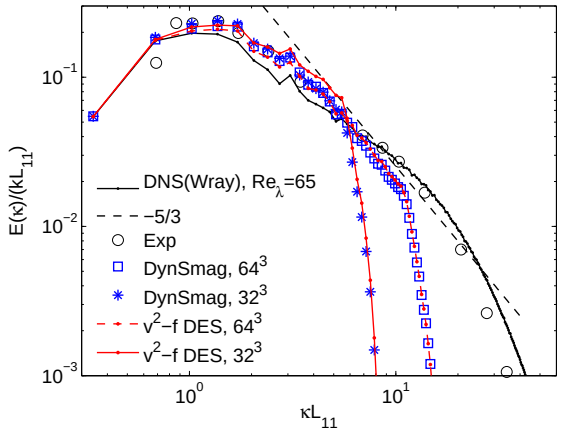


(c) LES and $v^2$-$f$ DES with $C_{\mathrm{DES}} = 0.8$ at $Re_\lambda = 65$

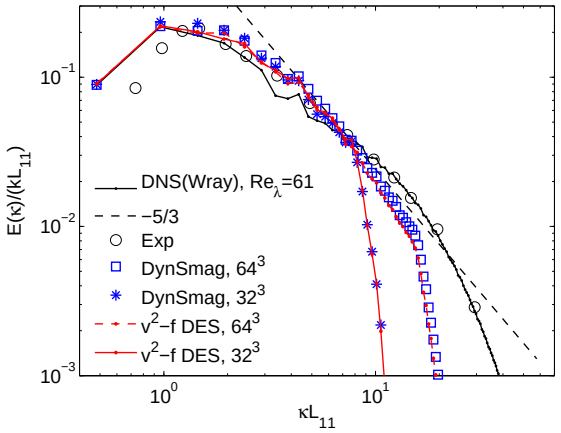


(d) LES and $v^2$-$f$ DES with $C_{\mathrm{DES}} = 0.8$ at $Re_\lambda = 61$

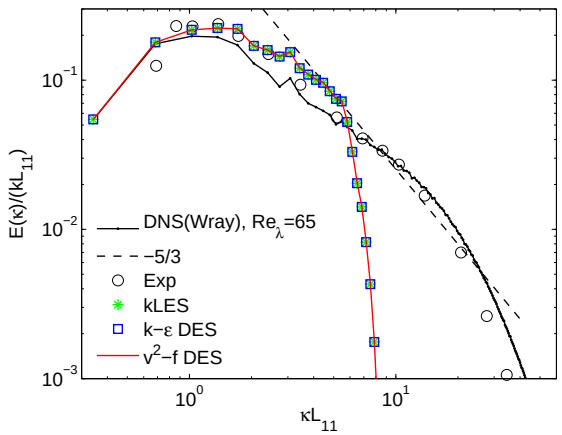


(e) sgs-$k$ LES, $k$-$\epsilon$ DES and $v^2$-$f$ DES with $C_{\mathrm{DES}} = 0.8$

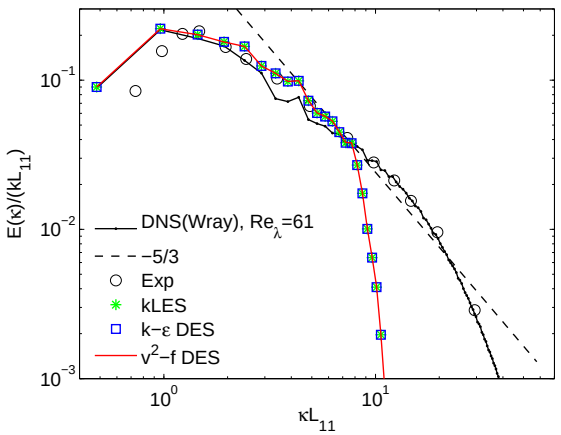


(f) sgs-$k$ LES, $k$-$\epsilon$ DES and $v^2$-$f$ DES with $C_{\mathrm{DES}} = 0.8$

Figure 4: Energy spectrum of decaying isotropic turbulence. The proposed $v^2$-$f$ DES model is simulated with three different values of $C_{\mathrm{DES}}$ on $32^3$ in (a) and (b). The curve labeled "-5/3" shows $E(\kappa) = C\epsilon^{2/3}\kappa^{-5/3}$ with the Kolmogorov constant $C = 1.5$. "DynSmag" indicates LES with the dynamic Smagorinsky model. The coefficient $C_{\mathrm{DES}} = 0.8$ is used for sgs-$k$ LES, $k$-$\epsilon$ DES and $v^2$-$f$ DES on $32^3$ in (e) and (f).

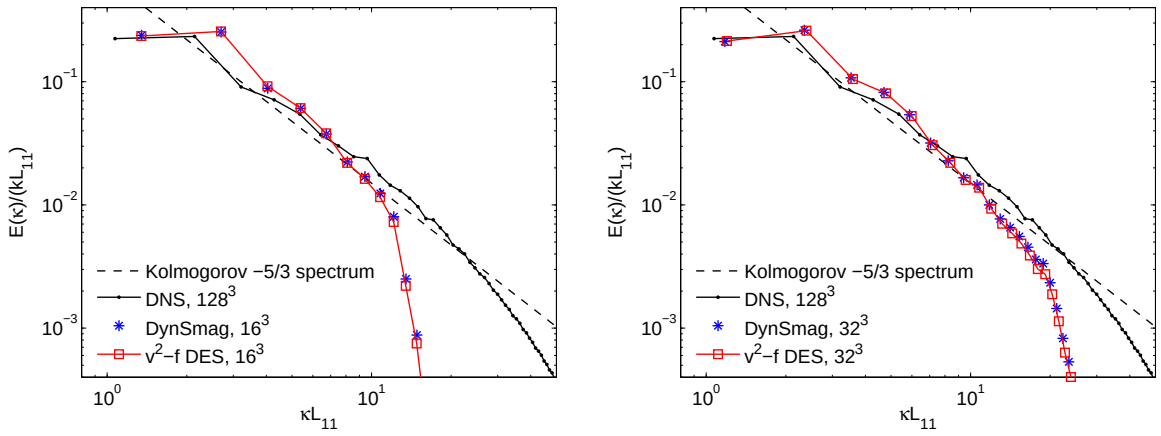


Figure 5: Energy spectrum of forced isotropic turbulence of $Re_\lambda = 98$. Shown are the present simulations of DNS, LES with the dynamic Smagorinsky model, and $v^2$-$f$ DES with $C_{\mathrm{DES}} = 0.8$ on the $16^3$ grid (left) and the $32^3$ grid (right).

# 3 Results: Flow over a circular cylinder

To test the LES mode of the proposed $v^2$-$f$ DES model, flow over a circular cylinder is chosen. The Reynolds number based on diameter $D$ is $Re_D = 3900$. The DES model coefficient $C_{\mathrm{DES}}$ was determined in isotropic turbulence. Therefore, it is imperative to test the DES model in anisotropic turbulence. The flow over a circular cylinder is a good test case, because this flow has been extensively studied both experimentally [24, 25] and numerically [19, 26, 24, 25]. Kravchenko and Moin [26] used a Galerkin B-spline method with the dynamic Smagorinsky model to simulate this flow and obtained good agreement of mean flow quantities with experimental data available at the time. Mahesh et al. [19] simulated this flow with the dynamic Smagorinsky model to validate the numerical method used in the CDP code. Dong et al. [24] performed DNS using a spectral element scheme on an unstructured grid and compared it with their PIV experiments. Recently, Parnaudeau et al. [25] performed an extensive study in order to address the lack of consensus in the literature for turbulence statistics immediately behind the cylinder. Parnaudeau et al. [25] simulated this flow with the dynamic Smagorinsky model using an immersed boundary method on uniform grids, and compared the computations with their PIV and hot-wire experiments.

The cylinder flow at $Re_D = 3900$ allows us to test DES as an LES model with grids appropriate for non-dissipative schemes. Strelets [27] and Travin et al. [28] performed SA-based DES for a cylinder at $Re_D = 50000$. We attempted this higher-$Re$ case first but discovered that the resolution used in the previous studies with dissipative upwind-biased schemes was inadequate for the present second-order non-dissipative code. Strelets used a hybrid central/upwind approximation [27], and Travin et al. used a fifth-order upwind scheme [28]. The resolution in Strelets [27] and Travin et al. [28] is even coarser than that in previous LES computations at $Re_D = 3900$ [29, 26, 19, 25]; Refs. [27, 28] used about 0.7 million points, whereas 1.3 - 4.4 million points are used in Refs. [29, 26, 19, 25]. Mittal and Moin [29] concluded that even a 5th-order upwind scheme can degrade LES computations at $Re_D = 3900$. Simulation of the $Re_D = 50000$ flow is still challenging with non-dissipative schemes. Because both $Re_D = 3900$ and 50000 are subcritical (turbulence develops after separation), the $Re_D = 3900$ flow is a good test case with grids appropriate for non-dissipative schemes. This test is not chosen to determine which DES model is better than others, since it is expected that all DES models will behave like the Smagorinsky model for this flow.

The present computation was performed on a domain whose inflow and outflow surfaces were $30D$ upstream and $35D$ downstream from the center of the cylinder, following the grid of Mahesh et al.[19]. The domain height was $50D$ and spanwise extent was $\pi D$. The size of the first grid cell adjacent to the cylinder is $0.0025D$ radially and $0.01D$ (or $0.57^\circ$) in the azimuthal direction $\theta$. The quadrilateral elements are approximately $0.04D \times 0.04D$ in the wake at a distance of $2D$ from the cylinder center. The current grid has slightly higher resolution on the wall than grids in previous LES studies [26, 19, 25] and less resolution than the DNS

study [24], particularly in the azimuthal $\theta$ and spanwise $z$ directions. There are about twenty grid points inside the boundary layer at separation. Fig. 6 shows the domain and the grid. The flow field is initially uniform. Without an imposed perturbation, the code generates 3D fluctuations due to biased round-off error. A statistically steady state is obtained after about 200 time units. Statistics were accumulated over approximately 30 vortex shedding cycles (140 time units) and over the spanwise direction. The time step is $\Delta_t = 0.001D/u_\infty$. Table 1 summarizes the computational parameters in the previous and current studies.

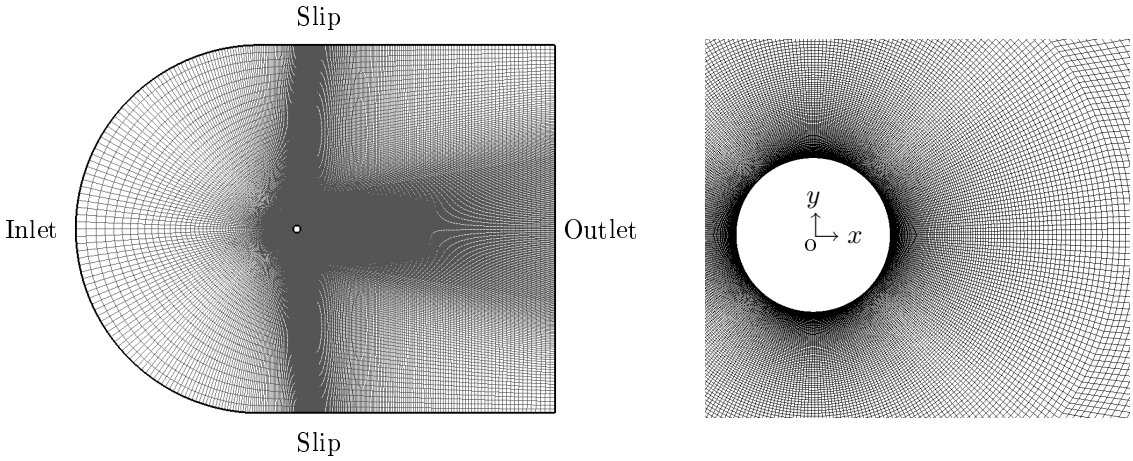


Figure 6: Computation domain (left) and grid around the cylinder (right).

| Study | Kravchenko et al. [26] | Mahesh et al. [19] | Parnaudeau et al. [25] | Dong et al. [24] | Present |
|---|---|---|---|---|---|
| Domain $[D]$ | $(R_d, L_z) = (30, \pi)$ | $L_{x,y,z} = (75, 50, \pi)$ | $L_{x,y,z} = (20, 20, \pi)$ | $L_{x,y,z} = (40, 18, \pi)$ | $L_{x,y,z} = (75, 50, \pi)$ |
| Grid | $n_{r,\theta,z} = (205, 185, 48)$ | $n_z = 32^*$ | $n_{x,y,z} = (961, 960, 48)^\dagger$ | $n_z = 128^\ddagger$ | $n_z = 64^*$ |
| $\Delta_{r,\theta}\|_{\text{wall}}$ $[10^{-2}D]$ | $(0.25, 1.7)$ | $(0.25, 1.2)^\S$ | $(2.1, 2.1)$ | $(0.36, 0.77)^\P$ | $(0.25, 1.0)^\|$ |
| $\Delta_t$ $[10^{-3}D/u_\infty]$ | 2.5 | 1 | 3 | 2 | 1 |
| Simulation type | LES | LES | LES | DNS | LES, DES |

Table 1: Computational parameters used for the current and previous studies. Note $^*$: unstructured quadrilateral grid with resolution of 0.04D for a distance of 1.5D in the wake, $^\dagger$: uniform mesh, $^\ddagger$: unstructured triangular grids, $^\S$: minimum values on the cylinder, $^\P$: calculated from their values in viscous wall units, $^\|$: uniform on the cylinder.

Three turbulence models are used for the present computations: dynamic-Smagorinsky LES [9], SA-based delayed DES (SA-DDES) [2] and the proposed $v^2$-$f$ DES model. For the dynamic Smagorinsky model, the ratio of test to grid filter widths is 2. The test filter is a top-hat filter which uses information from the neighboring grid cells. For SA-DDES, the SA equation without the trip term [4], called SA-noft2 in the turbulence community, is selected here because this version can use lower values of $\tilde{\nu}$ at freestream boundary [30]. The low-Reynolds number correction of Spalart et al. [2] is required for SA-DDES to compensate for unexpected activation of the wall functions possibly due to either low Reynolds number or very fine grids. This SA-DDES was also implemented in CDP. Using $C_{\text{DES}} = 0.65$ for SA-DDES gives the correct energy spectrum in isotropic turbulence (data not shown). $\Delta = \max(\Delta_i)$ in all cases. Initial and boundary conditions are listed in Table 2.

Instantaneous velocity and vorticity fields for the $v^2$-$f$ DES simulation are shown in Figs. 7 and 8, respectively. Fig. 7a shows the unsteady recirculation region behind the cylinder. Alternating regions of positive and negative cross-stream velocity are shown in Fig. 7b. These are related to Karman vortices shown in Fig. 8. Fig. 7c clearly shows fluctuating spanwise velocity which indicates three dimensional flow structures in the wake. Figs. 7 and 8 are similar to the LES results of Kravchenko et al., i.e., Figs. 2-5 of Ref. [26], which show the similar structures.

Mean flow fields are obtained from the simulation over approximately 30 vortex shedding cycles and over the spanwise direction in the near wake of the cylinder. Fig. 9 shows the results of $v^2$-$f$ DES. The velocity deficit in the wake is well shown in Fig. 9a with the negative bubble near the cylinder. Separating shear layer

| Variables | All | $v^2$-$f$ DES | | | | SA-DDES |
|---|---|---|---|---|---|---|
| | $u_i$ | $k$ | $\overline{v^2}$ | $\epsilon$ | $f$ | $\tilde{\nu}$ |
| Initial Conditions | uniform $u_\infty$ | $10^{-3}u_\infty^2$ | $(2/3)\times 10^{-3}u_\infty^2$ | $10^{-3}u_\infty^3/D$ | none | $5\nu$ |
| Wall Boundary | 0 | 0 | 0 | $\nu\partial_n^2 k$ | 0 | 0 |
| Inlet Boundary | $u_\infty$ | 0 | 0 | zero gradient | zero gradient | $0.5\nu$ |
| Outlet Boundary | convective outlet | | | | zero gradient | convective outlet |
| Slip Boundary | zero gradient | | | | | |
| Z planes | periodic | | | | | |

Table 2: Initial and Boundary conditions in the present computations. The gradient $\partial_n$ is in the wall normal direction.

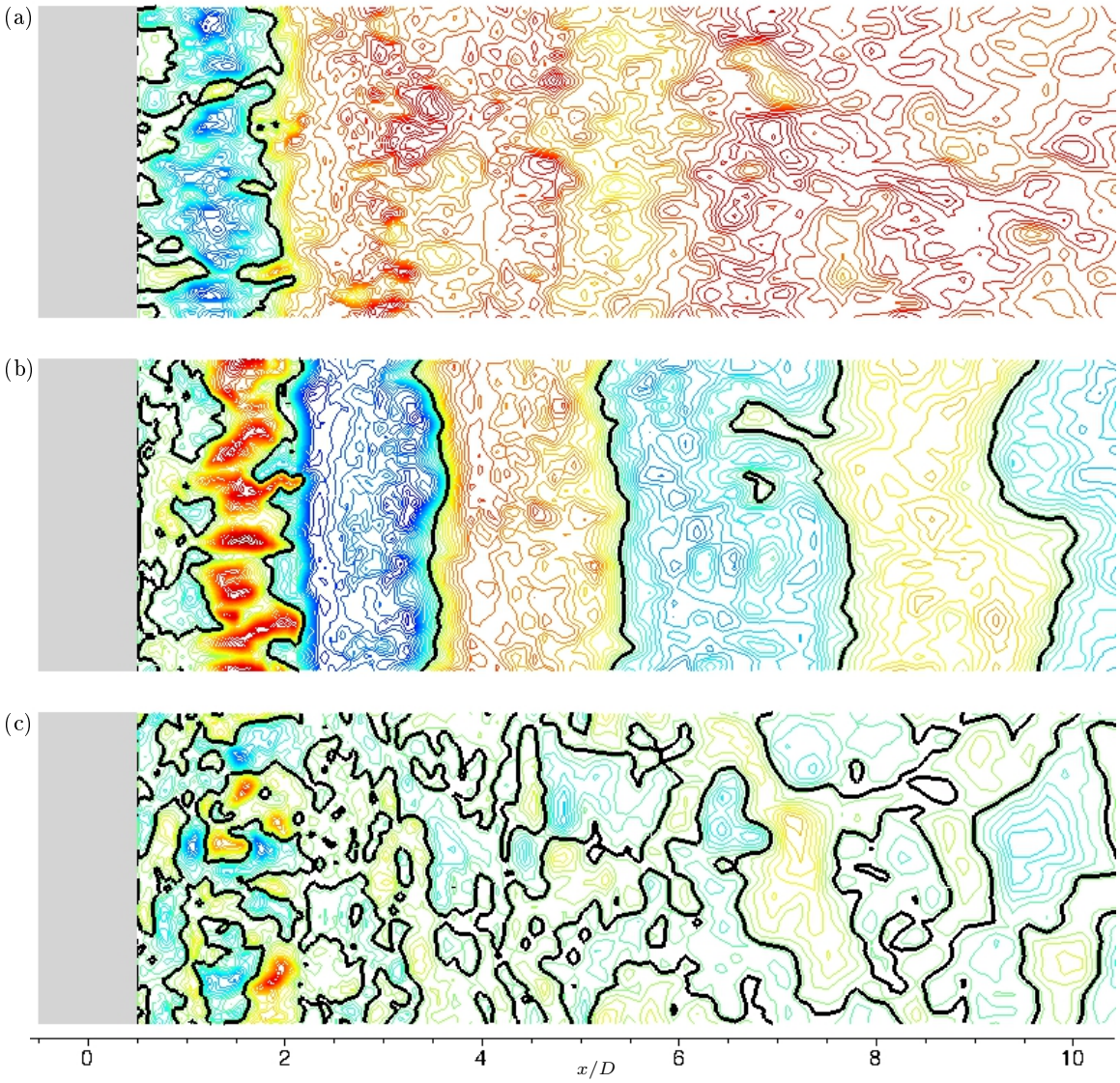


Figure 7: Instantaneous velocity fields in the $y = 0$ plane in the wake of a circular cylinder at $Re_D = 3900$ from the $v^2$-$f$ DES simulation. Shown are the normalized streamwise velocity $u/u_\infty$ (a), the normalized cross-flow velocity $v/u_\infty$ (b), and the normalized spanwise velocity $w/u_\infty$ (c). The thick black lines indicate the zero value. The number of color contour levels is 52 between $-1.5$ (blue) and 1.5 (red).

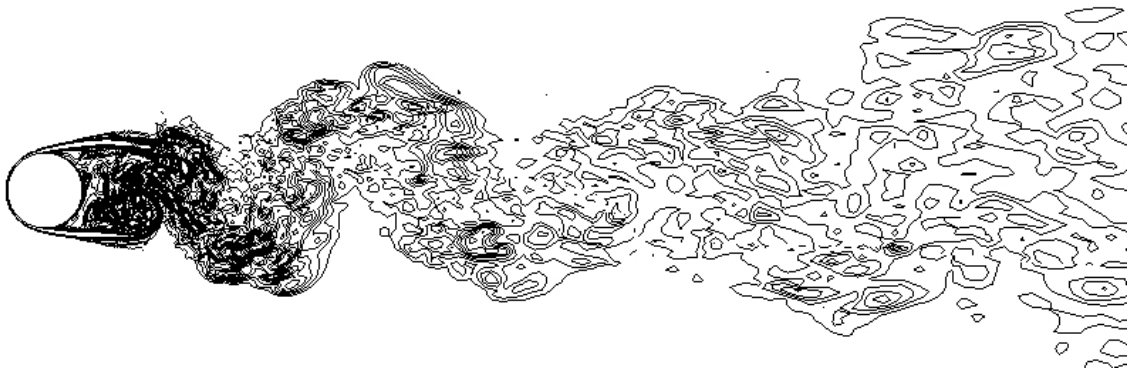

Figure 8: Instantaneous vorticity magnitude $\omega D/u_\infty$ on a $x$-$y$ plane with 16 contours from $\omega D/u_\infty = 0.5$ to $\omega D/u_\infty = 10.0$ in the simulation of $v^2$-$f$ DES.

is clearly shown in the spanwise vorticity field, Fig. 9b. The Reynolds shear stress $\langle u'v' \rangle$ is anti-symmetric with respect to the centerline (see Fig. 9c). $\langle u'v' \rangle$ has has two dominant peaks of $|\langle u'v' \rangle| = 0.119$ at $x/D = 2.08$ and two secondary peaks of $|\langle u'v' \rangle| = 0.040$ at $x/D = 1.37$. The r.m.s. streamwise velocity $u_{\rm rms}$ in Fig. 9d shows a strong gradient in the separating shear layers and two maxima associated with the vortex formation in Fig. 9b. These mean flow structures are qualitatively similar to Parnaudeau et al.[25]'s experimental and LES data, and Dong et al. [24]'s experimental and DNS data. Fig. 10 presents current simulation results with fewer contour lines for direct comparison among the three models. In general, all three models provide the similar mean flow fields with subtle differences. The simulation without any turbulence model is not included in Fig. 10 because its results are simply not correct (see Table 3).

Integral flow quantities are well predicted by all three models, as listed in Table 3. The drag coefficient $C_D = 1.00$ of $v^2$-$f$ DES matches well with previous experiment data [26] and computations [19]. The value $C_D = 0.965$ predicted by SA-DDES is acceptable. The base pressure coefficient $C_{p,b} = -0.928$ of $v^2$-$f$ DES is most similar to that of Kravchenko et al. [26]. SA slightly underestimates $C_{p,b}$, and, without any turbulence model, $C_{p,b}$ is simply wrong. The separation point $\theta_{\rm sep} = 87.1$ of the present dynamic-Smagorinsky LES and $v^2$-$f$ DES is in the range of the experimental data set and similar to previous LES results [26, 19, 25]. Previous studies have a broad range of values for the recirculation length $L_R$; this value is sensitive to experimental conditions [25], and previous LES slightly underestimated this value. The current value $L_R = 1.44$ of $v^2$-$f$ DES is in the range of the experimental data. The Strouhal number $St$ is the least sensitive quantity in Table. 3. The current LES, $v^2$-$f$ DES and even the simulation with no model predict the shedding frequency very accurately. SA-DDES slightly overestimates $St$. The minimum streamwise velocity $U_{\rm min}$ predicted by all the present computations is within the range of the previous data.

Fig. 11 shows mean velocity profiles in the wake. $v^2$-$f$ DES predicts the centerline mean streamwise velocity with slightly better prediction downstream $5 < x/D < 10$ than the other present computations (Fig. 11a). All current LES and DES's reproduce the mean streamwise and cross-flow velocity at three locations in the wake as shown in Figs. 11b and 11c. For the mean cross-flow velocity $V$ at $x/D = 1.54$, the present dynamic-Smagorinsky LES and $v^2$-$f$ DES provide a better match to the experiment of Parnaudeau et al. than does the LES of Parnaudeau et al. [25] .

Fig. 12 shows Reynolds stress profiles in the near wake. Overall, all three models predict the three components quite well compared with the LES and experimental data of Parnaudeau et al. [25]. At $x/D = 1.54$, $v^2$-$f$ DES and the present dynamic-Smagorinsky LES are slightly better than SA-DDES, particularly for $\langle u'u' \rangle$ and $\langle u'v' \rangle$. For $\langle u'u' \rangle$, $v^2$-$f$ DES and the present dynamic-Smagorinsky LES match closer with the experiment of Parnaudeau et al. [25] than does their LES, similar to $V$ in Fig. 11c. Such better prediction in the present simulation is probably due to better resolution very near the cylinder; the present grid is finer than that of Parnaudeau et al. [25] from the cylinder surface to $x/D \simeq 1.2$ in the wake.

Compared to $v^2$-$f$ DES and dynamic-Smagorinsky LES, SA-DDES predicts more smoothed-out profiles of $V$, $\langle u'u' \rangle$, and $\langle u'v' \rangle$ in the near wake. This is related to large mean eddy viscosity $\langle \nu_t \rangle$ produced by SA-DDES, as shown in Fig. 13. $v^2$-$f$ DES and dynamic-Smagorinsky LES generate $\langle \nu_t \rangle \sim \nu$ in the near

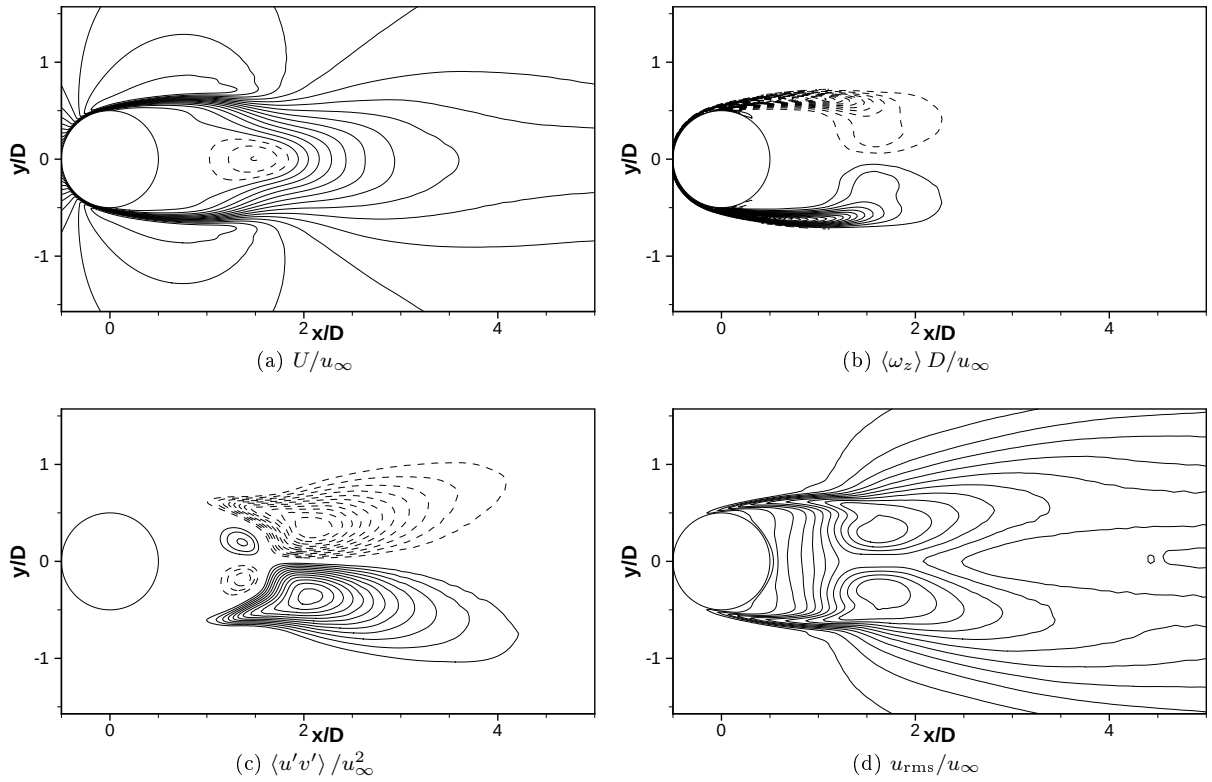


(a) $U/u_\infty$ (b) $\langle\omega_z\rangle D/u_\infty$

(c) $\langle u'v'\rangle/u_\infty^2$ (d) $u_{\rm rms}/u_\infty$

Figure 9: Mean flow fields in the $v^2$-$f$ DES simulation: (a) normalized streamwise velocity with contour levels of $U/u_\infty|_{\rm min} = -0.3$ and $|\Delta U/u_\infty| = 0.1$; (b) normalized spanwise vorticity with contour levels of $|\langle\omega_z\rangle D/u_\infty|_{\rm min} = 1$ and $|\Delta\langle\omega_z\rangle D/u_\infty| = 1$; (c) normalized Reynolds stress with contour levels of $|\langle u'v'\rangle/u_\infty^2|_{\rm min} = 0.018$ and $|\Delta\langle u'v'\rangle/u_\infty^2| = 0.009$; and (d) normalized r.m.s. streamwise velocity with contour levels of $u_{\rm rms}/u_\infty|_{\rm min} = 0.04$ and $|\Delta u_{\rm rms}/u_\infty| = 0.04$. In all plots, dashed lines indicate a negative value.

| | Study | $C_D$ | $C_{p,b}$ | $\theta_{\rm sep}$ | $L_R/D$ | $St$ | $U_{\rm min}/u_\infty$ |
|---|---|---|---|---|---|---|---|
| Exp. | Data set* | 0.99±0.05 | -0.88±0.05 | 86.0±2 | 1.4±0.1 | 0.215±0.005 | -0.24±0.01 |
| | Parnaudeau et al. [25] | | | 88 | 1.51 | 0.208±0.002 | -0.34 |
| | Dong et al. [24] | | | | 1.47 | | -0.252 |
| DNS | Dong et al. [24] | | -0.88 | | 1.36 | 0.20 | -0.291 |
| LES | Kravchenko et al. [26] | 1.04 | -0.94 | 88.0 | 1.35 | 0.210 | -0.37 |
| | Mahesh et al. [19] | 1.00 | | 87.6 | 1.35 | 0.218 | -0.31 |
| | Parnaudeau et al. [25] | | | 87.6 | 1.35 | 0.208 | -0.31 |
| | Present | 0.994 | -0.881 | 87.1 | 1.48 | 0.214 | -0.320 |
| DES | Present, $v^2$-$f$ DES | 1.00 | -0.928 | 87.1 | 1.44 | 0.214 | -0.304 |
| | Present, SA-DDES | 0.965 | -0.969 | 88.3 | 1.37 | 0.221 | -0.283 |
| | Present, w/o turb. model | 1.18 | -1.16 | 89.4 | 0.841 | 0.214 | -0.264 |

Table 3: Mean flow quantities of the flow around the circular cylinder at $Re_D = 3900$: the drag coefficient $C_D$, the base pressure coefficient $C_{p,b}$, the separation angle from the front $\theta_{\rm sep}$, the recirculation length $L_R$, the Strouhal number $St$, and the minimum streamwise velocity $U_{\rm min}$ on the centerline. Note *: experimental data in Table II of Kravchenko et al. [26]

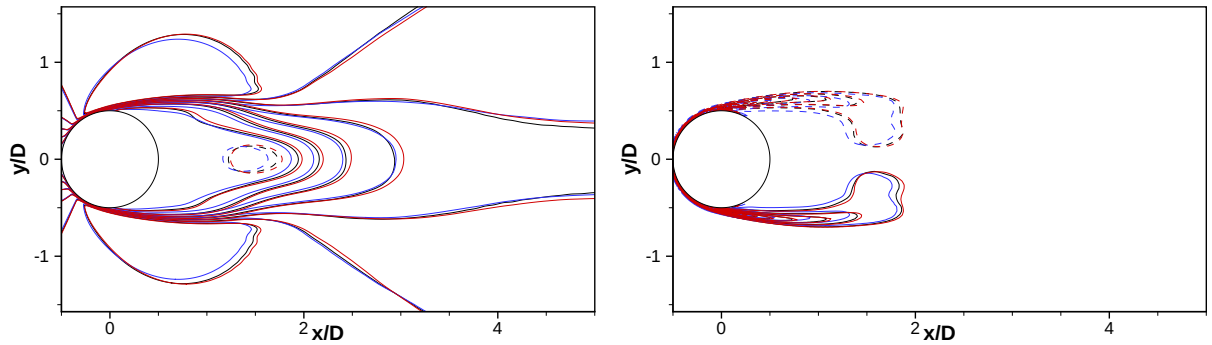


(a) $U/u_\infty$ (b) $\langle\omega_z\rangle D/u_\infty$

(c) $\langle u'v'\rangle/u_\infty^2$ (d) $u_{\mathrm{rms}}/u_\infty$

Figure 10: Mean flow fields in the $v^2$-$f$ DES simulation (–), dynamic-Smagorinsky LES (–), and SA-DDES (–): (a) normalized streamwise velocity with contour levels of $U/u_\infty|_{\mathrm{min}} = -0.2$ and $|\Delta U/u_\infty| = 0.2$; (b) normalized spanwise vorticity with contour levels of $|\langle\omega_z\rangle D/u_\infty|_{\mathrm{min}} = 2$ and $|\Delta\langle\omega_z\rangle D/u_\infty| = 4$; (c) normalized Reynolds stress with contour levels of $|\langle u'v'\rangle/u_\infty^2|_{\mathrm{min}} = 0.018$ and $|\Delta\langle u'v'\rangle/u_\infty^2| = 0.036$; and (d) normalized r.m.s. streamwise velocity with contour levels of $u_{\mathrm{rms}}/u_\infty|_{\mathrm{min}} = 0.08$ and $|\Delta u_{\mathrm{rms}}/u_\infty| = 0.12$. In all plots, dashed lines indicate a negative value.

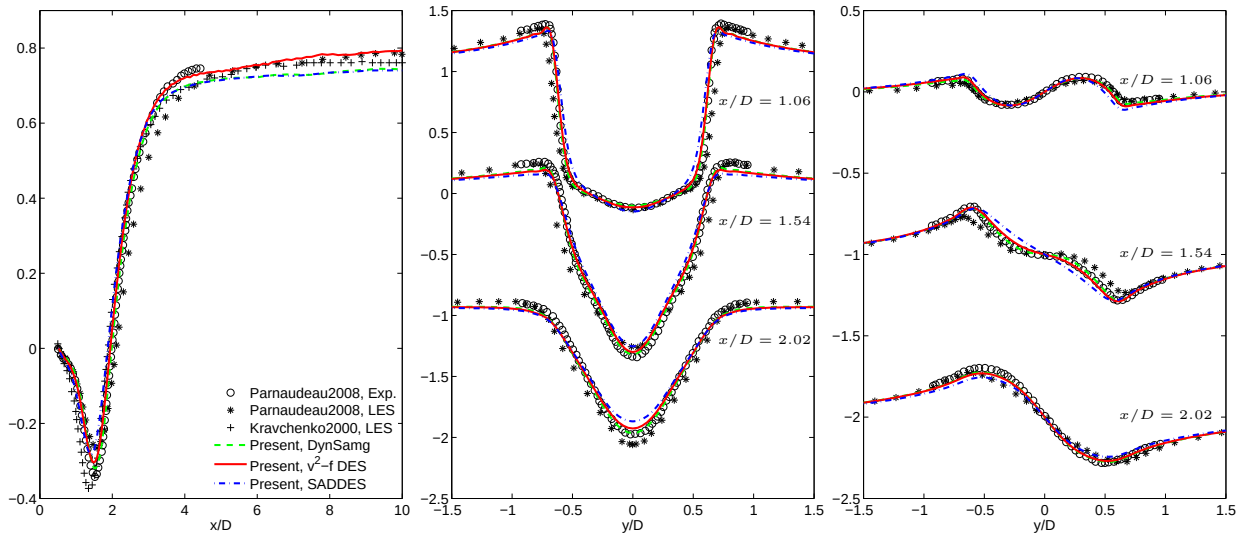


(a) $U/u_\infty$ (b) $U/u_\infty$ (c) $V/u_\infty$

Figure 11: Mean velocity profiles in the wake of the circular cylinder at $Re_D = 3900$. Shown are (a) normalized streamwise velocity $U/u_\infty$ on the centerline, and (b) $U/u_\infty$ and (c) normalized cross-flow velocity $V/u_\infty$ at three locations in the wake of a circular cylinder at $Re_D = 3900$. In (b) and (c), profiles at $x/D = 1.54$ and $x/D = 2.02$ are vertically shifted down by 1 and 2, respectively.

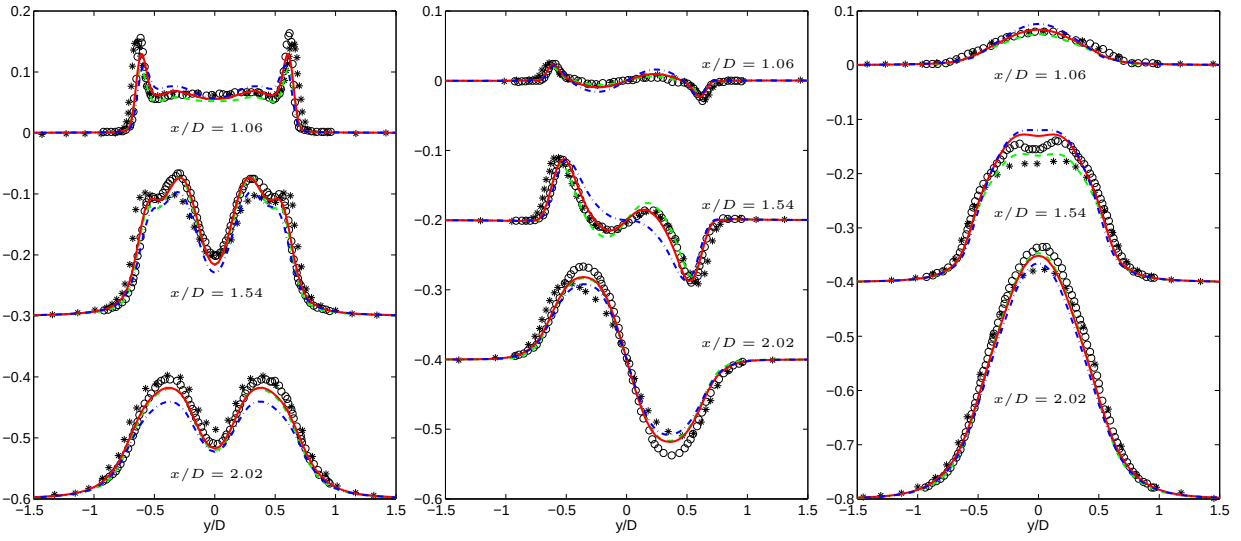


(a) $\langle u'u' \rangle / u_\infty^2$ (b) $\langle u'v' \rangle / u_\infty^2$ (c) $\langle v'v' \rangle / u_\infty^2$

Figure 12: Normalized Reynolds stress profiles at three locations in the near wake of a circular cylinder at $Re_D = 3900$. Note the obvious vertical shifts for the profiles at $x/D = 1.54$ and 2.02. See Fig. 11 for labels.

wake around $1 \lesssim x/D \lesssim 2$, whereas $\langle \nu_t \rangle \sim 2\nu$ from SA-DDES. Interestingly, both $v^2$-$f$ DES and SA-DDES have two peaks around $x/D \simeq 1.5$ close to the centerline, whereas the dynamic Smagorinsky has two peaks off the centerline at $x/D \simeq 2.5$ and $y/D \simeq \pm 0.5$. Although $v^2$-$f$ DES damps $\langle \nu_t \rangle$ downstream of $x/D \gtrsim 2$, this does not significantly affect the mean flow field in the far wake (see Fig. 15).

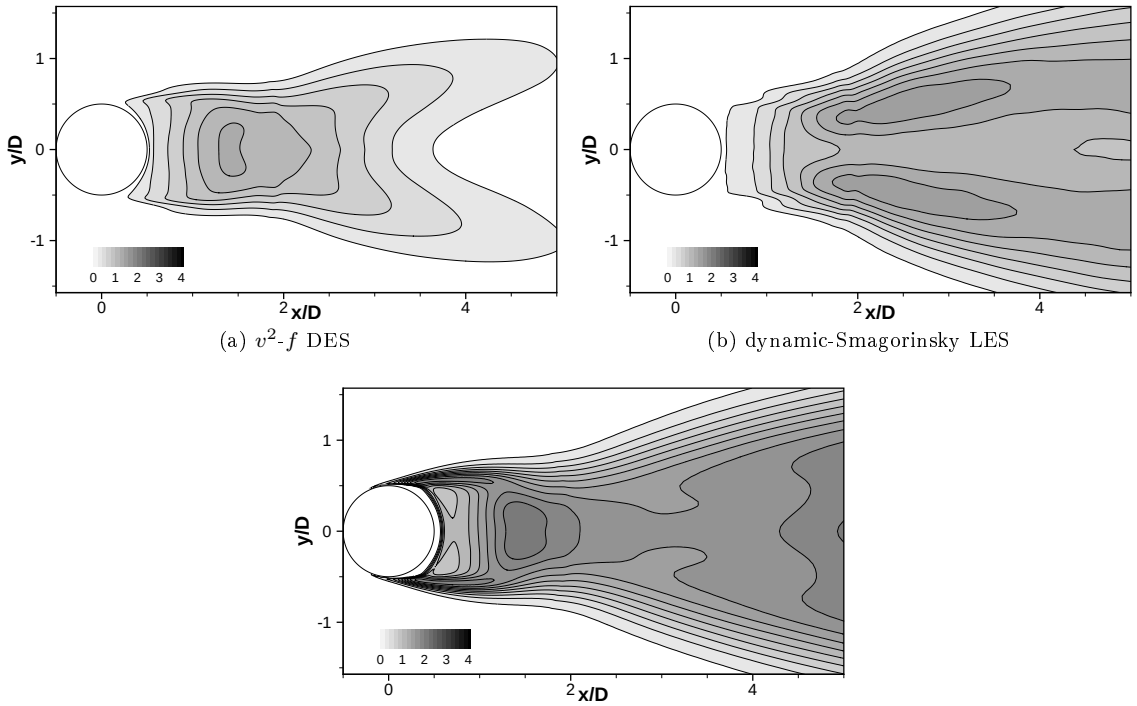


(a) $v^2$-$f$ DES

(b) dynamic-Smagorinsky LES

(c) SA-DDES

Figure 13: Contours of the normalized mean eddy viscosity $\langle \nu_t \rangle / \nu$. In all plots, $\langle \nu_t \rangle / \nu|_{\min} = 0.2$ and $|\Delta \langle \nu_t \rangle / \nu| = 0.2$.

Fig. 14 shows mean model quantities of the $v^2$-$f$ DES model. Overall, a similar structure is observed in $\langle k \rangle$, $\left\langle \overline{v^2} \right\rangle$, and $\langle \epsilon_{\mathrm{DES}} \rangle$; they are symmetric with respect to the centerline with two peaks around $x/D \sim 1.5$ near the centerline. The mean function $\langle f \rangle$ has peaks similar to those of $\left\langle \overline{v^2} \right\rangle$, which visually shows that $f$ suppresses $\overline{v^2}$ near the wall and produces $\overline{v^2}$ away from the wall.

Mean flow quantities in the far wake are shown in Fig. 15. Only the data of Kravchenko et al.[26] is included as the reference, because Parnaudeau et al.[25] did not include far wake data. Data of Kravchenko et al.[26] has good agreement with the experiment of Ong and Wallace [31]. Similar to the near wake, all three turbulence models give the acceptable profiles. $v^2$-$f$ DES has slightly better agreement in $\langle u'v' \rangle$ than the others, whereas dynamic Smagorinsky is slightly better for $\langle u'u' \rangle$. Based on both $\langle u'u' \rangle$ and $\langle v'v' \rangle$, this far-wake flow is still far from isotropic turbulence.

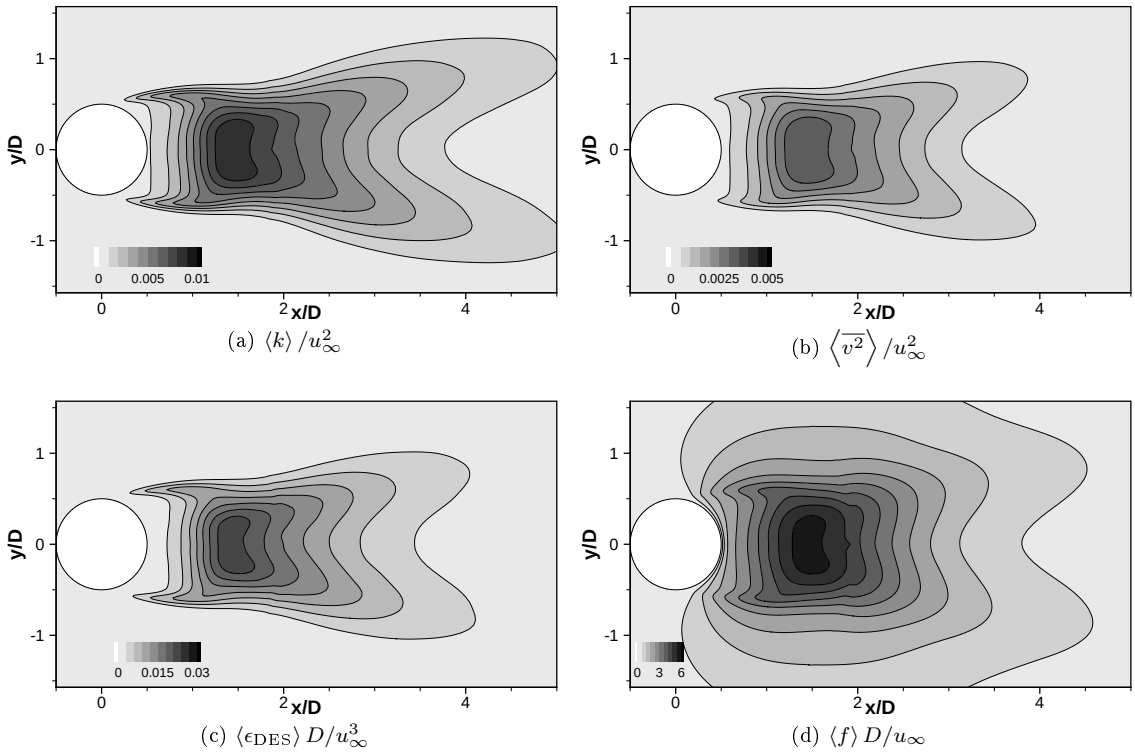


(a) $\langle k \rangle / u_\infty^2$ (b) $\left\langle \overline{v^2} \right\rangle / u_\infty^2$

(c) $\langle \epsilon_{\mathrm{DES}} \rangle D / u_\infty^3$ (d) $\langle f \rangle D / u_\infty$

Figure 14: Normalized mean model quantities of the $v^2$-$f$ DES model. (a) $|\Delta \langle k \rangle / u_\infty^2| = 0.001$. (b) $|\Delta \left\langle \overline{v^2} \right\rangle / u_\infty^2| = 0.005$. (c) $|\Delta \langle \epsilon_{\mathrm{DES}} \rangle D / u_\infty^3| = 0.003$. (d) $|\Delta \langle f \rangle D / u_\infty| = 0.6$.

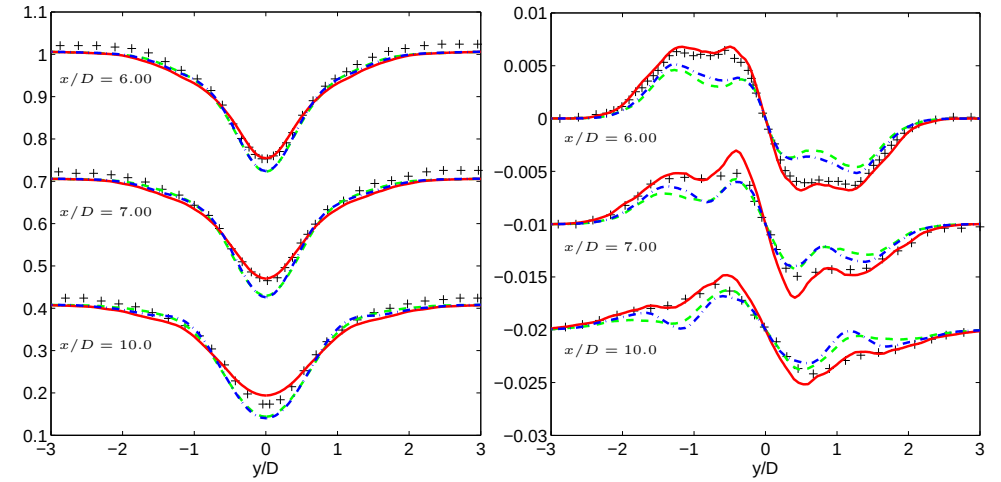


(a) $U/u_\infty$ (b) $\langle u'v' \rangle / u_\infty^2$

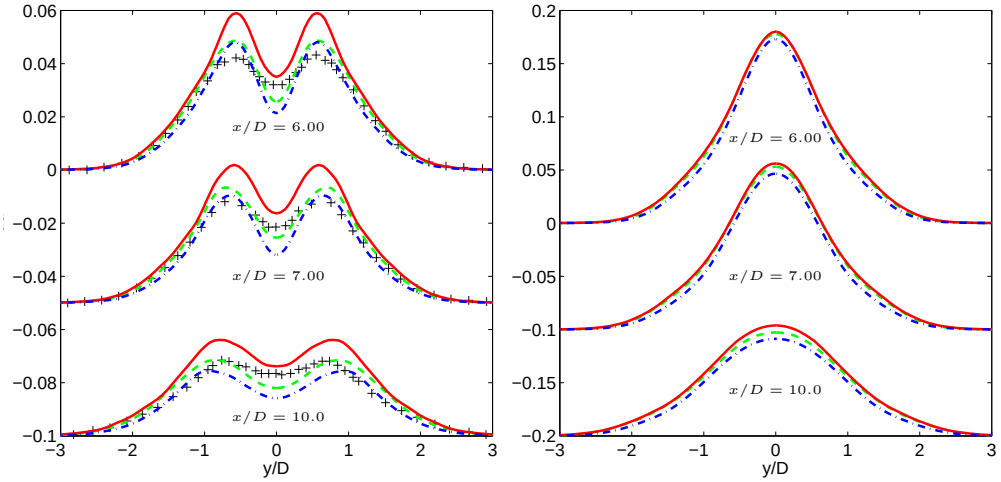


(c) $\langle u'u' \rangle / u_\infty^2$ (d) $\langle v'v' \rangle / u_\infty^2$

Figure 15: Mean streamwise velocity (a), Reynolds shear stress $\langle u'v' \rangle$ (b), and normal stresses $\langle u'u' \rangle$ (c) and $\langle v'v' \rangle$ (d), at three locations in the far wake of a circular cylinder at $Re_D = 3900$. Note the obvious vertical shifts for the profiles at $x/D = 7.00$ and 10.0. See Fig. 11 for labels.

# 4 Conclusions and Future Work

DES based on the $v^2$-$f$ model was proposed, implemented in the unstructured incompressible code CDP, and tested for isotropic turbulence and flow around a circular cylinder. Three coefficients in the elliptic relaxation equation of the original RANS model are modified in order that $\overline{v^2}$ is statistically $(2/3)k$ in the limit of isotropic turbulence. This allows the $v^2$-$f$ DES formulation to reduce to sgs-$k$ LES in this limit. The DES coefficient $C_{\mathrm{DES}}$ determined from isotropic turbulence is $C_{\mathrm{DES}} = 0.8$.

Flow around a circular cylinder at $Re_D = 3900$ is simulated with the proposed $v^2$-$f$ DES along with SA-based DDES and the dynamic Smagorinsky model. Since at this Reynolds number turbulence occurs after separation, this case tests only the LES mode. $v^2$-$f$ DES reproduces not only instantaneous large structures in the wake but also mean flow fields as observed in previous experimental and numerical studies. Dynamic-Smagorinsky LES and SA-DDES are performed for direct comparison among the three models. Overall, all three turbulence models accurately predict integral quantities, mean velocity profiles and turbulence intensity profiles in the wake. Although some quantities are predicted slightly better by a particular model, the difference is not sufficient enough for one to assert that one of the models is the best. The largest difference among the models appears in the turbulent viscosity, which is presumably related to subtle differences in the presented statistics. For subcritical Reynolds numbers, it is expected that all DES models should behave like a good LES model. Further numerical tests, specifically, for wall bounded internal flows where turbulent separation and reattachment locations are more difficult to predict, remain for future study.

# References


[1] P. R. Spalart, W. H. Jou, M. Strelets, and S. R. Allmaras. *Comments on the feasibility of LES for wings and on a hybrid RANS/LES approach*. Greyden Press, 1997.

[2] P. R. Spalart, S. Deck, M. L. Shur, K. D. Squires, M.K. Strelets, and A. Travin. A new version of detached-eddy simulation, resistant to ambiguous grid densities. *Theoretical and Computational Fluid Dynamics*, 20(3):181–195, July 2006.

[3] P. R. Spalart. Detached-eddy simulation. *Annual Review of Fluid Mechanics*, 41:181–202, 2009.

[4] P. R. Spalart and S. R. Allmaras. A one-equation turbulence model for aerodynamics flows. *La Recherche Aérospatiale*, 1:5–21, 1994.

[5] F. S. Lien, G. Kalitzin, and P. A. Durbin. RANS modeling for compressible and transitional flows. In *Proceedings of the Summer Program*. Center for Turbulence Research, Stanford, 1998.

[6] P. A. Durbin and B. A. Pettersson Reif. *Statistical Theory and Modeling for Turbulent Flows*, chapter 7.3 and 7.4. Wiley, 2001.

[7] G. Iaccarino, C. Marongiu, P. Catalano, and M. Amato. RANS simulation of the separated flow over a bump with active control. Technical report, Center for Turbulence Research, Stanford University, 2003.

[8] G. Constantinescu, M. Chapelet, and K. Squires. Turbulence modeling applied to flow over a sphere. *AIAA J.*, 41:1733–1742, 2003.

[9] Massimo Germano, Ugo Piomelli, Parviz Moin, and William H. Cabot. A dynamic subgrid-scale eddy viscosity model. *Physics of Fluids A: Fluid Dynamics*, 3(7):1760–1765, 1991.

[10] P. A. Durbin. On the $k$-$\epsilon$ stagnation point anomaly. *Int. Journal of Heat and Fluid Flow*, 17:89–90, 1996.

[11] Fue-Sang Lien and Georgi Kalitzin. Computations of transonic flow with the v2-f turbulence model. *International Journal of Heat and Fluid Flow*, 22:53–61, 2001.

[12] Brian E. Launder. Second-moment closure:present... and future? *International Journal of Heat and Fluid Flow*, 10(4):282 – 300, 1989.

[13] Juan C. del Alamo and Javier Jimenez. Direct numerical simulation of the very large anisotropic scales in a turbulent channel. Technical report, Center for Turbulence Research Annual Research Briefs. Stanford University, 2001. pp. 329-341.

[14] Juan C. del Alamo and Javier Jimenez. Spectra of the very large anisotropic scales in turbulent channels. *Physics of Fluids*, 15(6):L41–L44, 2003.

[15] Juan C. del Alamo, Javier Jimenez, Paulo Zandonade, and Robert D. Moser. Scaling of the energy spectra of turbulent channels. *J. Fluid Mech.*, 500:135–144, 2004.

[16] Sergio Hoyas and Javier Jimenez. Scaling of the velocity fluctuations in turbulent channels up to $Re_\tau = 2003$. *Physics of Fluids*, 18(1):011702, 2006.

[17] Akira Yoshizawa. A statistically-derived subgrid model for the large-eddy simulation of turbulence. *Physics of Fluids*, 25(9):1532–1538, 1982.

[18] F. Ham and G. Iaccarino. Energy conservation in collocated discretization schemes on unstructured meshes. *Center of Turbulence Research Annual Research Briefs*, pages 3–14, 2004.

[19] K. Mahesh, G. Constantinescu, and P. Moin. A numerical method for large-eddy simulation in complex geometries. *Journal of Computational Physics*, 197(1):215 – 240, 2004.

[20] A. A. Wray. Hom02: Decaying isotropic turbulence. In *A Selection of Test Cases for the Validation of Large-Eddy Simulations of Turbulent Flows*. AGARD Advisory Report No 345, 1997.

[21] G. Comte-Bellot and S. Corrsin. Simple Eulerian time correlation of full- and narrow-band velocity signals in grid-generated 'isotropic' turbulence. *J. Fluid Mech.*, 48:273–337, 1971.

[22] V. Eswaran and S. B. Pope. An examination of forcing in direct numerical simulations of turbulence. *Computers & Fluids*, 16(3):257–278, 1988.

[23] S. Tavoularis, J. C. Bennett, and S. Corrsin. Velocity-derivative skewness in small Reynolds number, nearly isotropic turbulence. *Journal of Fluid Mechanics*, 88(01):63–69, 1978.

[24] S. Dong, G. E. Karniadakis, A. Ekmekci, and D. Rockwell. A combined direct numerical simulation–particle image velocimetry study of the turbulent near wake. *Journal of Fluid Mechanics*, 569:185–207, 2006.

[25] Philippe Parnaudeau, Johan Carlier, Dominique Heitz, and Eric Lamballais. Experimental and numerical studies of the flow over a circular cylinder at Reynolds number 3900. *Physics of Fluids*, 20(8):085101, 2008.

[26] Arthur G. Kravchenko and Parviz Moin. Numerical studies of flow over a circular cylinder at $Re_D = 3900$. *Physics of Fluids*, 12(2):403–417, 2000.

[27] M. Strelets. Detached eddy simulation of massively separated flows. In *39th AIAA Aerosp. Sci. Meet. Exhib.*, number AIAA 2001-0879, 2001.

[28] A. Travin, M. Shur, M. Strelets, and P. Spalart. Detached-eddy simulations past a circular cylinder. *Flow Turbulence and Combustion*, 63(1-4):293–313, 1999.

[29] R. Mittal and P. Moin. Suiability of upwind-biased finite-difference shcemes for large-eddy simulation of turbulent flows. *AIAA J.*, 35:1415–1417, 1997.

[30] P. R. Spalart and C. L. Rumsey. Effective inflow conditions for turbulence models in aerodynamic calculations. *AIAA Journal*, 45(10):2544–2553, October 2007.

[31] L. Ong and J. Wallace. The velocity field of the turbulent very near wake of a circular cylinder. *Experiments in Fluids*, 20(6):441–453, April 1996.